AFRL-OSR-VA-TR-2013-0093

Mesoscopi Detailed Balance Algorithms for Quantum and Classical Turbulence

Vahala

College of William & Mary

FEBRUARY 2013
Final Report

AIR FORCE RESEARCH LABORATORY
AF OFFICE OF SCIENTIFIC RESEARCH (AFOSR)/RSL
ARLINGTON, VIRGINIA 22203
**AIR FORCE MATERIEL COMMAND**

REPORT DOCUMENTATION PAGE

Public reporting burden for this collection of information is estimated to average 1 hour per response, including the time for reviewing instructions, searching existing data sources, gathering and maintaining the data needed, and completing and reviewing this collection of information. Send comments regarding this burden estimate or any other aspect of this collection of information, including suggestions for reducing this burden to Department of Defense, Washington Headquarters Services, Directorate for Information Operations and Reports (0704-0188), 1215 Jefferson Davis Highway, Suite 1204, Arlington, VA 22202-4302. Respondents should be aware that notwithstanding any other provision of law, no person shall be subject to any penalty for failing to comply with a collection of information if it does not display a currently valid OMB control number. **PLEASE DO NOT RETURN YOUR FORM TO THE ABOVE ADDRESS.**

1. REPORT DATE *(DD-MM-YYYY)* 15-10-2012	2. REPORT TYPE Final Performance		3. DATES COVERED *(From - To)* 07-01-2008 to 12-31-2012
4. TITLE AND SUBTITLE Mesoscopi Detailed Balance Algorithms for Quantum and Classical Turbulence			5a. CONTRACT NUMBER FA9550-09-1-0607
			5b. GRANT NUMBER
			5c. PROGRAM ELEMENT NUMBER
6. AUTHOR(S) George Vahala			5d. PROJECT NUMBER
			5e. TASK NUMBER
			5f. WORK UNIT NUMBER
7. PERFORMING ORGANIZATION NAME(S) AND ADDRESS(ES) College of William & Mary Williamsburg, VA 23185			8. PERFORMING ORGANIZATION REPORT NUMBER
9. SPONSORING / MONITORING AGENCY NAME(S) AND ADDRESS(ES) Air Force Office of Scientific Research Dr. Fariba Fahroo 875 North Randolph St., Suite 325, Romm 3112 Arlington, VA 22203			10. SPONSOR/MONITOR'S ACRONYM(S) RSL
			11. SPONSOR/MONITOR'S REPORT NUMBER(S) AFRL-OSR-VA-TR-2013-0093

12. DISTRIBUTION / AVAILABILITY STATEMENT

Distribution A: Approved for Public Release

13. SUPPLEMENTARY NOTES

14. ABSTRACT

Qubit unitary algorithms are a novel computational scheme for the solution of nonlinear problems of physics. Not only are they ideally parallelized on classical supercomputers but will be immediately applicable to quantum computers when eventually they become available. Specific sequences of collide-stream-rotate unitary operators will yields, in the field theoretic limit, representations of the one-dimensional Magnetohydrodynamics-Burgers equations, KdV and nonlinear Schrodinger equations. Generalizing to three dimensions, quantum turbulence is examined for the (scalar) Gross-Pitaevskii equation. Initial conditions were determined under which the Poincare recurrence of the Hamiltonian states were unexpectedly short. Triple energy cascade regions were determined for the compressible kinetic energy. The unitary algorithm ia readily extended to spinor Bose-Einstein condensate. The code has shown ideal parallelization to over 275 000 cores, permitting production runs on grids far exceeding those achievable by standard computational algorithms.

15. SUBJECT TERMS

qubits, unitary, turbulence, energy spectra

16. SECURITY CLASSIFICATION OF:			17. LIMITATION OF ABSTRACT	18. NUMBER OF PAGES	19a. NAME OF RESPONSIBLE PERSON
a. REPORT U	b. ABSTRACT U	c. THIS PAGE U		26	19b. TELEPHONE NUMBER *(include area code)*

1. Introduction

Qubit unitary algorithms are a novel computational scheme for the solution of nonlinear problems of physics. Not only are they idealized parallelized on classical supercomputers but will be immediately applicable to quantum computers when they come on line.

While a binary bit can take on only the values "0" or "1", the qubit resides on a surface of the unit sphere with state $|q\rangle = \alpha_0|0\rangle + \alpha_1|1\rangle$, a superposition of states $|0\rangle$ and $|1\rangle$. The (complex_ probability amplitudes $|\alpha_0|^2 + |\alpha_1|^2 = 1$.
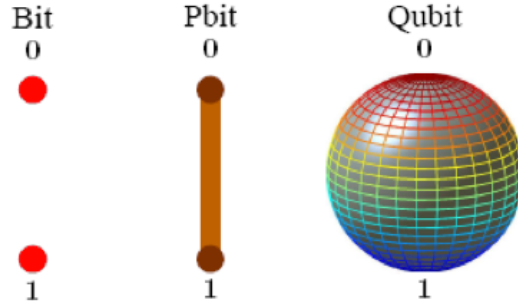
Fig. 1   A schematic of a bit, a probability-bit 'Pbit', and a qubit.

Things get more interesting when one considers the interaction of two qubits :

$$|q_1 q_2\rangle = \alpha_{00}|00\rangle + \alpha_{01}|01\rangle + \alpha_{10}|10\rangle + \alpha_{11}|11\rangle \quad , \quad \text{with} \quad \sum |\alpha_{ij}|^2 = 1$$

Of much importance in quantum information is qubit correlations – i.e., quantum entanglement. It is this feature that permits quantum information to solve problems like n-digit factorization into two prime number that scale polynomially in n (Shor algorithm) while on classical supercomputers the scaling is exponential in n.

The typical quantum lattice algorithm for the evolution of a scalar mesoscopic field is the introduction of 2 qubits per lattice node. One then introduces an appropriate sequence of unitary collide-stream operations that entangle the on-site qubits and then streams this entangled information to neighboring lattice sites. This sequence of collide-stream unitary operations has been mimicked in some successful NMR experiments by the Cory group [xxx]. In particular, since a unitary operator *U* is related to a Hamiltonian *H* by $U = \exp(iH)$, the NMR experimentalists and readily determine the NMR pulses and their durations in order to emulate the desired unitary operations. Thus, from the qubit unitary algorithm for the one-dimensional (1D) Burgers equation

$$\frac{\partial u}{\partial t} + u\frac{\partial u}{\partial x} = v\frac{\partial^2 u}{\partial x^2}$$

one can immediate determine the required electromagnetic pulses and polarizations. In 2004, using 16 lattice sites, with 2 qubits/site, the Cory group could reproduce the early stage of the steepening of a sinusoidal wave front towards a shock. The dashed points are experimental data while the continuous curve is the analytic solution to the Burgers equation
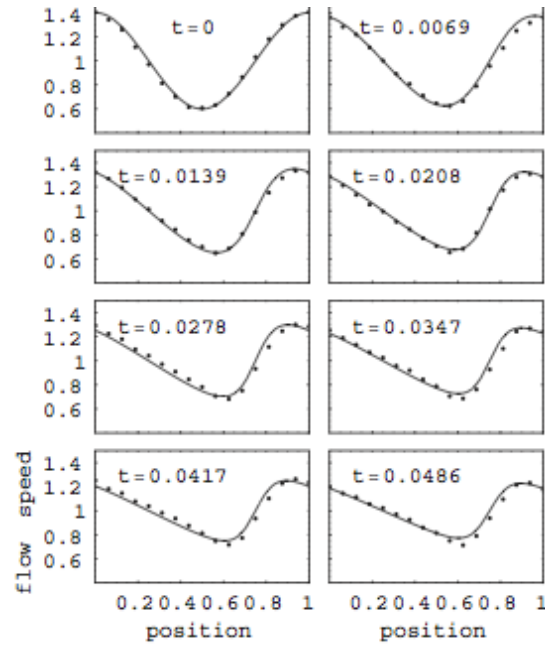
Fig. 2 A comparison between theoretical (lines) and NMR data points in the early stages of shock development in the solution of the 1D Burgers equation. The NMR pulse sequence is determined from the Hamiltonian representation of the unitary collide-stream operators of the qubit algorithm that solves the Burgers equation.

It is also of interest to consider some of the ideas being put forward for a quantum computer. In particular the Zoller group (PRL – 2008, 2011) has proposed using the alkaline earth atom ^{87}Sr in their Bose-Einstein condensate optical lattices.
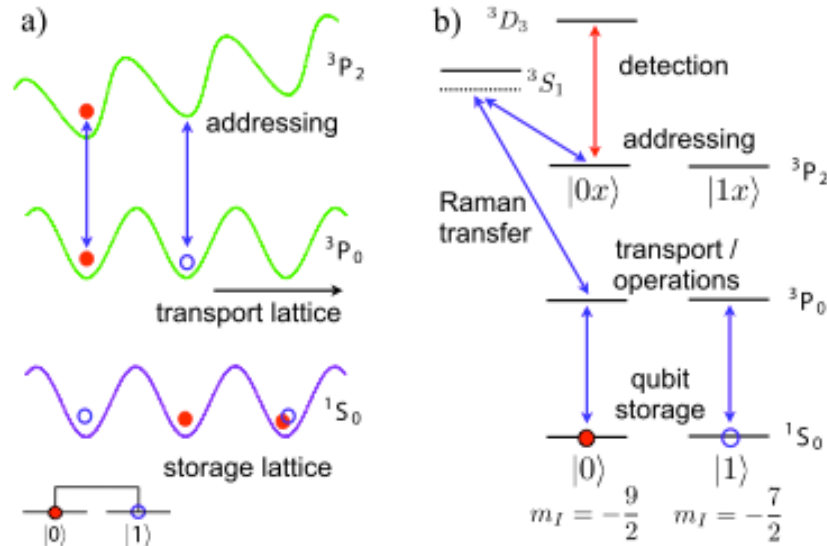

Fig. 3 Quantum computing with independent lattices: (a) qubits in long-lived states in a storage lattice are transferred to a completely independent transport lattice for operations between distant qubits, or addressed individually by coupling to a level that is shifted by a gradient magnetic field.

(b) This is accomplished by encoding qubits in nuclear spin states, producing independent lattice for the $^1S_0$ and $^3P_0$ levels, and using $^3P_2$ for individual addressing.

One can readily encode qubits in the nuclear spin states with different magnetic quantum numbers m_I – in particular one can define $|0\rangle \triangleq |^1S_0, m_I = -\frac{9}{2}\rangle$, and the state $|1\rangle \triangleq |^1S_0, m_I = -\frac{7}{2}\rangle$, Fig. 3b. These are quite stable states since they are very insensitive to magnetic field fluctuations. Moreover quantum tunneling is negligible resulting in deep optical lattices for storage and transport lattices.   We thus see some similarity with these ideas of developing a quantum computer and the use of unitary operators for shifting qubits and collisional coupling of qubits.

2. 1D Quantum Lattice Algorithms for Classical Solitons

We have investigated quantum unitary algorithms for both the 1D Korteweg-de-Vries and the Nonlinear Schrodinger equations [G. Vahala, J. Yepez and L. Vahala, Phys. Lett. **A310**, 187-196 (2003)]. In particular to recover the 1D nonlinear Schrodinger equation for bright solitons

$$i\frac{\partial \psi}{\partial t} = -\frac{\partial^2 \psi}{\partial x^2} - |\psi|^2 \psi \tag{1}$$

we introduced 2 qubits/lattice site and employed the following sequence of unitary collide-stream operators on the spinor

$$|\psi(t)\rangle = \begin{pmatrix} \alpha \\ \beta \end{pmatrix} \tag{2}$$

to obtain the spinor evolution equation

NLS: $\quad |\psi(t+\Delta t)\rangle = S_2^T C S_2 C . S_2^T C S_2 C . S_1^T C S_1 C . S_1^T C S_1 C \; |\psi(t)\rangle \tag{3}$

where the unitary S_1-operator streams the probability amplitude α, while S_2 streams β. The unitary collision operator C is known as the square-root-of-swap:

NLS: $\quad C = \frac{1}{2}\begin{pmatrix} 1-i & 1+i \\ 1+i & 1-i \end{pmatrix} \tag{4}$

since

$$C^2 \begin{pmatrix} \alpha \\ \beta \end{pmatrix} = \begin{pmatrix} \beta \\ \alpha \end{pmatrix} \qquad \text{with} \quad C^4 = I \tag{5}$$

(Here *I* is the identity matrix).

On the otherhand, to recover the KdV equation

$$\frac{\partial \psi}{\partial t} + \psi \frac{\partial \psi}{\partial x} + \frac{\partial^3 \psi}{\partial x^3} = 0 \tag{6}$$

with the nonlinear convective term $\psi\, \partial \psi / \partial x$, the omission of the standard 2nd derivative but the appearance now of the 3rd derivative, the unitary collide-stream algorithm interwines the streaming on the two probability amplitudes

KdV: $\quad |\psi(t+\Delta t)\rangle = S_1 C^T S_2^T C . S_1^T C^T S_2 C . S_1^T C S_2 C^T . S_1 C S_2^T C^T \; |\psi(t)\rangle \tag{7}$

The unitary collision operator is now the square-root-of-NOT

KdV: $C = \dfrac{1}{\sqrt{2}} \begin{pmatrix} 1 & 1 \\ -1 & 1 \end{pmatrix}$, with $C^4 = -I$. (8)

The beauty of these 1D solition solutions is that their solutions, though nonlinear, have an arbitrary scaling parameter:

NLS: $\psi_{NLS}(x,t) = \sqrt{2}\, a\,.\,Exp\left[i\left\{ \dfrac{bx}{\sqrt{2}} - \left(\dfrac{b^2}{4} - a^2 \right)t \right\} \right]\, .\, Sech\left[a\left(\sqrt{2}\,x - bt \right) \right]$ (9)

where a and b are free parameters, controlling the soliton amplitude and velocity. For the KdV-soliton, there is still one free parameter which couples the soliton amplitude and velocity.

KdV: $\psi_{KdV}(x,t) = \dfrac{1}{2}a\, Sech^2\left[\dfrac{\sqrt{a}}{2}(x - at) \right]$ (10)

3. Qubit Unitary Algorithms for 3D and 2D Quantum Turbulence

Bose-Einstein Condensates (BECs) of weakly interacting dilute gases are playing an extremely important role in both atomic and condensed matter research. If the BEC is in a magnetic trap, then the spin is aligned to the magnetic field and the mean field representation of the evolution of the ground state is given by the Gross-Pitaevskii (GP) equation for the single-atom wavefunction

$$i\frac{\partial \psi(\mathbf{x},t)}{\partial t} = \left[-\nabla^2 - \mu + g|\psi(\mathbf{x},t)|^2 \right]\psi(\mathbf{x},t)$$ (11)

μ is the chemical potential and the nonlinear term $g|\psi|^2\psi$ arises from the weak s-wave Boson interactions. Under the Madelung transformation, the GP Eq. (11) can be written in fluid-like variables of mean density $\rho(\mathbf{x},t)$ and mean superfluid velocity $\mathbf{u}_s(\mathbf{x},t)$:

$$\psi(\mathbf{x},t) = \sqrt{\rho(\mathbf{x},t)}\,\exp\left[i\varphi(\mathbf{x},t) \right]$$
$$\mathbf{u}_s(\mathbf{x},t) = \nabla\varphi$$ (12)

with

$$\frac{\partial \rho}{\partial t} + \nabla\cdot(\rho\mathbf{u}_s) = 0 \quad, \text{ and } \quad \rho\left(\frac{\partial}{\partial t} + \mathbf{u}_s\cdot\nabla \right)\mathbf{u}_s = \nabla p + \nabla\cdot\vec{\vec{\Sigma}} \quad,$$ (13)

and barotropic pressure : $p \sim g\rho^2$. Thus the GP-BEC ground state corresponds to the dynamics of a *compressible*, inviscid Euler-like superfluid, but with a novel quantum stress tensor

$$\Sigma_{ij} = \rho\,\frac{\partial^2 \ln\rho}{\partial x_i\,\partial x_j} \quad.$$ (14)

It was finally determined that the Bose-Einstein ground state wave function is, in fact, an order parameter, with a topological singularity at $\psi = 0$. This topological singularity is nothing but the core of a quantum vortex with mean density $\rho = 0$.

Experimentally, the trapped BEC was subject to rotation. When the angular momentum had reached a threshold value, line vortices appeared within the BEC – the number of such vortices being dependent on the value of the angular momentum since all quantum vortices have the same strength

$$\oint \mathbf{u}_s \cdot d\ell = n\kappa \qquad (15)$$

Indeed, from the BEC density data, one finds the formation of a vortex lattice as the BEC is rotated with higher angular momentum:
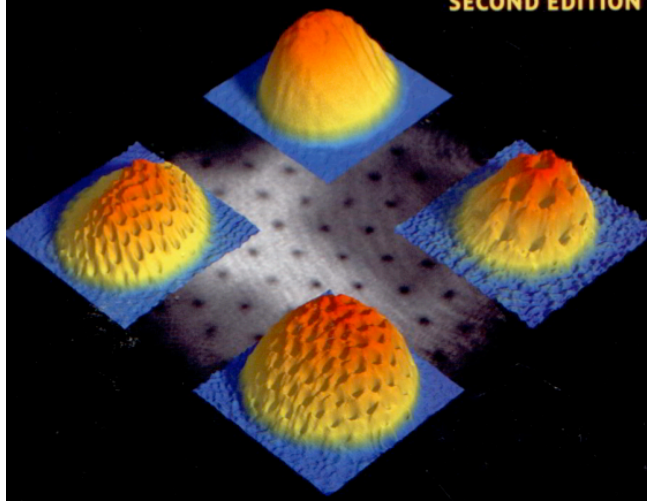

Fig. 4 The formation of a BEC vortex lattice as the BEC is rotated more rapidly. The quantum vortex can be readily identified by the zero density at the quantum vortex core, which in these plots of the BEC density show up as cavities: at the top, the BEC rotation is too low for the existence of a quantum vortex. Moving clockwise, one finds 16 quantum cores, then 70 quantum cores and finally 130 quantum cores [from Ketterle et. al.]

There are considerable differences between a quantum vortex and a classical vortex:

(a) a classical vortex can exist in an incompressible fluid, but the quantum vortex is essentially compressible (since $\rho = 0$ at the vortex core),

(b) the presence of viscosity is essential for classical vortex reconnection, while quantum vortex reconnection occurs without viscosity due to the topological singularity at the vortex core and the novel quantum stress tensor $\overset{\leftrightarrow}{\Sigma}$.

(c) classical vortices (or eddies) can have a continuous range of values for circulation, and this play a significant role in kinetic energy cascades: in 3D, energy cascades from large sale eddies to small scale eddies till viscosity eventually destroys the smallest scale eddies and dissipates them into heat. On the otherhand, quantum vortices are identical, with the same quantized circulation strength, Eq. (15). Moreover, it is energetically unfavorable for the persistence of high winding number vortices: $\psi = \sqrt{\rho} \exp(in\varphi), n \geq 2$. These degernate winding-number n vortices rapidly split into n winding number-1 vortices. This is readily seen in our simulations, Fig. 5, which show the evolution of quantum line vortex core isosurfaces for a degenerate initial winding number $n = 5$. Initially, there are 4 such line vortices in each 2D-plane for a total of 12 vortices, Fig. 5a. The bounds on the color scheme on the vortex core isosurface are: blue for the isosurface $\varphi = 0 \,(\mathrm{mod}\ 2\pi)$, while $\varphi \to 2\pi \,(\mathrm{mod}\ 2\pi)$ isosurface is in red. The 5-fold periodicity is evident. On the walls, we plot the phase information of the wavefunction as it intercepts the boundaries. From this, the topological singularity $(\rho = 0)$ acts like a branch-point singularity, Eq. (12), with 5 branch cuts connecting each quantum vortex core intercept with the boundaries. Very rapidly, Fig. 5b, these degenerate isosurfaces split into winding number-1 vortices (as can be

readily seen from the phase information on the walls and the single branch cut joining the singular vortex cores. The oscillations on the vortex cores are due to the excitation of Kelvin waves – and this we will discuss later.
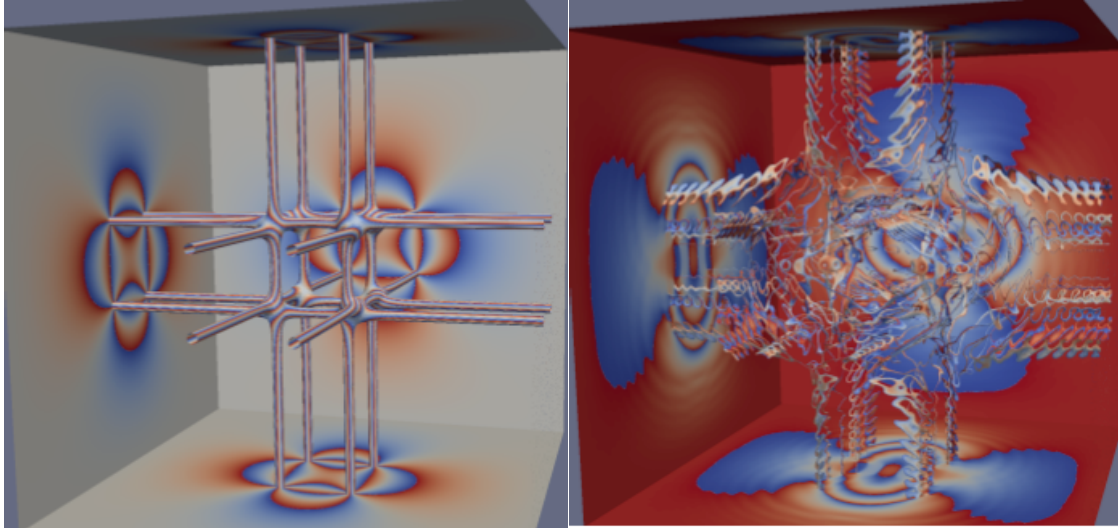

(a)   t = 0   (b)   t = 3000

Fig. 5 The splitting of the 5-fold degenerate quantum vortices, (a), into 5 non-degenerate quantum vortex cores, (b). Lattice grid 2048^3. Phase information on both the topological quantum vortex cores and the walls : $\varphi = 0(blue)$, $\varphi = 2\pi(red)$. The oscillations on the vortex cores as seen in (b) are due to Kelvin waves.

(d)   in the case of classical vortices the evolution equations are dissipative, while the BEC quantum vortex evolution is determined by a conservative (non-dissipative) Hamiltonian system.

Feynmann put forth the definition that quantum turbulence arises with a 3D tangle of quantized vortices, Fig. 6
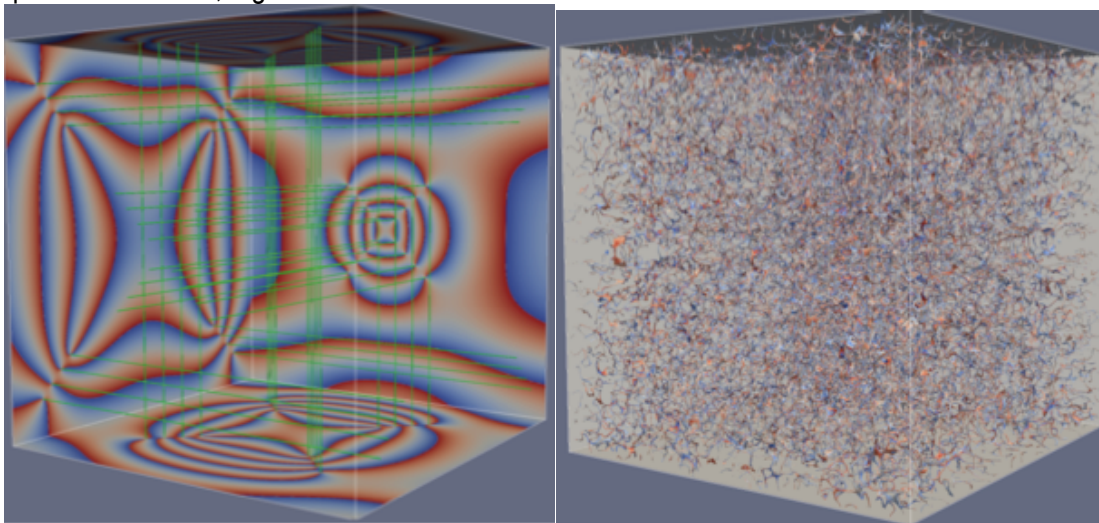
(a)   t = 0 quantum core isosurfaces   (b) later turbulent state of tangled quantum vortices

Fig. 6 Evolution of quantum turbulence, defined as a tangle of quantum vortices.

4. Qubit Unitary Lattice Algorithm for Quantum Turbulence

To develop an algorithm for the 3D scalar GP Eq. (11), we need introduce just the minimal 2 qubits/spatial node with its Hilbert space of dimension 2^2 - i.e., the states $|00\rangle$, $|01\rangle$, $|10\rangle$, $|11\rangle$ - and focus on the probability amplitudes for the two states $|10\rangle$ and $|01\rangle$. Let us denote these probabilities at spatial grid point $\mathbf{x}$ at time t as $\alpha(\mathbf{x},t)$ and $\beta(\mathbf{x},t)$ and consider the spinor field

$$|\psi(\mathbf{x},t)\rangle = \begin{pmatrix} \alpha(\mathbf{x},t) \\ \beta(\mathbf{x},t) \end{pmatrix} \tag{16}$$

We now consider the interleaved unitary collide-stream operator sequence for spatial direction $\hat{\mathbf{x}}$

$$I_{x,\sigma} = S_{-\Delta x,\sigma} C\, S_{\Delta x,\sigma} C \qquad , \qquad \sigma = 0\,,1 \quad , \tag{17}$$

where the unitary collision operators that entangles locally the amplitudes is our $\sqrt{SWAP}$-gate, Eq. (4), and the unitary streaming operator that spreads this entanglement to the nearby lattice sites is given by

$$S_{\Delta x,0}|\psi(\mathbf{x})\rangle = \begin{pmatrix} \alpha(\mathbf{x}+\Delta x\hat{\mathbf{x}}) \\ \beta(\mathbf{x}) \end{pmatrix} \quad , \quad S_{\Delta x,1}|\psi(\mathbf{x})\rangle = \begin{pmatrix} \alpha(\mathbf{x}) \\ \beta(\mathbf{x}+\Delta x\hat{\mathbf{x}}) \end{pmatrix} \tag{18}$$

For 3D, the full unitary evolution operator is

$$U[\Omega] = I_{x0}^2\, I_{y1}^2\, I_{z0}^2 \exp\left[-i\frac{\varepsilon^2\Omega(\mathbf{x})}{2}\right] \cdot I_{z1}^2\, I_{y0}^2\, I_{x1}^2 \exp\left[-i\frac{\varepsilon^2\Omega(\mathbf{x})}{2}\right] \tag{19}$$

where we have introduced a phase rotation factor $\varepsilon^2\Omega(\mathbf{x})$, with $\varepsilon \ll 1$.

The mesoscopic qubit lattice time evolution algorithm is thus

$$|\psi(\mathbf{x},t+\Delta t)\rangle = U[\mathbf{x},\Omega]\,|\psi(\mathbf{x},t)\rangle \tag{20}$$

In the spatial continuum limit, $\Delta x = O(\varepsilon)$, this reduces to the spinor equation

$$|\psi(\mathbf{x},t+\Delta t)\rangle = |\psi(\mathbf{x},t)\rangle - i\varepsilon^2\left[-\sigma_x\nabla^2 + \Omega(\mathbf{x})\right]|\psi(\mathbf{x},t)\rangle + O(\varepsilon^4) \tag{21}$$

where σ_x is the Pauli spin matrix

$$\sigma_x = \begin{pmatrix} 0 & 1 \\ 1 & 0 \end{pmatrix} .$$

Thus, under diffusion ordering,

$$\Delta t \sim \Delta x^2 \sim O(\varepsilon^2) \tag{22}$$

and taking moment contraction of the spinor field in order to recover the scalar order parameter wavefunction $\psi(\mathbf{x},t)$:

$$\varepsilon \rightarrow 1 \tag{23}$$

we obtain the desired GP equation for $\psi(\mathbf{x},t)$

$$i\frac{\partial\psi(\mathbf{x},t)}{\partial t} = -\nabla^2\psi(\mathbf{x},t) - a\left[1 - g|\psi(\mathbf{x},t)|^2\right]\psi(\mathbf{x},t) + O(\varepsilon^2) \tag{24}$$

on identifying $\Omega \rightarrow g|\psi|^2$.

• *Exact Conservation of the Mean Density*

Since the qubit lattice algorithm is unitary, the norm of the spinor $|\psi\rangle$ is automatically conserved. However, there can be fluctuations in the mean density $\langle\rho\rangle = \int d^3\mathbf{x}|\psi(\mathbf{x},t)|^2$ if there is overlap in the components of the 2-spinor

$$\langle\delta\rho\rangle = \int d^3\mathbf{x}\left(|\psi(\mathbf{x},t)|^2 - \langle\psi|\psi\rangle\right) = \int d^3\mathbf{x}\left(\alpha^\dagger\beta + \alpha\beta^\dagger\right)$$

Thus, if α is purely imaginary and β is purely real (or vice versa), then the overlap between the two components vanish and $\langle\delta\rho\rangle = 0$.

This is readily accomplished in the algorithm by special initialization of the wave function. In particular, given the complex BEC ground state wave function $\psi(\mathbf{x},t=0) = \alpha(\mathbf{x},0) + \beta(\mathbf{x},0)$, we simply choose

$$\alpha(\mathbf{x},0) \triangleq i\, Im\,\psi(\mathbf{x},0) \quad , \quad \beta(\mathbf{x},0) \triangleq Re\,\psi(\mathbf{x},0) \tag{25}$$

We also need to generalize the phase rotation operator Ω to the non-diagonal potential matrix

$$\vec{\Omega} = \begin{pmatrix} \cos\left(|\psi|^2\right) & -i\sin\left(|\psi|^2\right) \\ -i\sin\left(|\psi|^2\right) & \cos\left(|\psi|^2\right) \end{pmatrix} \tag{26}$$

so that

$$\sum_\gamma \left(\vec{\Omega} \cdot |\psi\rangle\right)_\gamma = \exp\left[-i|\psi^2|\right]\psi \tag{27}$$

on setting $\varepsilon \to 1$.

5. Scaling of the Qubit Lattice Algorithm on Various Architectures

While all our production runs have been performed at the DoD supercomputer sites, the scaling experiments where performed on the larger DoE supercomputers at Argonne (IBM/Blue Gene), Oak Ridge (the CRAY Jaguarpf → Titan) and Oakland (NERSC CRAY Hopper). In particular, using a coupled BEC qubit unitary algorithm we have achieved excellent strong and weak scaling.

In strong scaling, the grid is held fixed while one increasing the number of processors. Ideal scaling would result in a proportional decreasing in the wall clock time. On the Oak Ridge CRAY, we have close to perfect scaling to 276 480 cores tested.

Strong Scaling: Grid 8400^3, CRAY XK-6 (Titan/Jaguarpf)

#processors	Wall-clock (s)	Speed-up	Ideal Speed-up
96 000	1422.2	1	1
120 000	1087.9	1.25	1.25
150 000	872.9	1.63	1.56
180 000	729.3	1.95	1.88
210 000	643.5	2.21	2.19
216 000	628.6	2.26	2.25

Strong Scaling: Grid 9600^3, CRAY XK-6 (Titan/Jaguarpf)

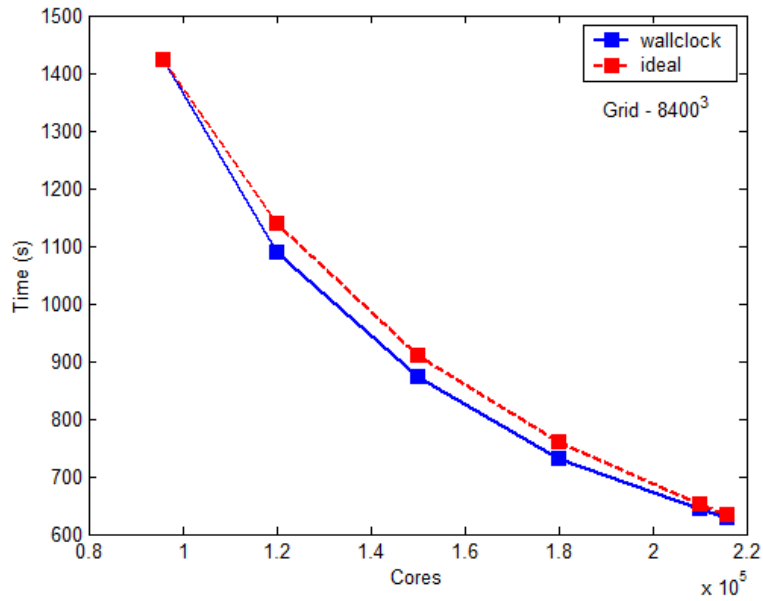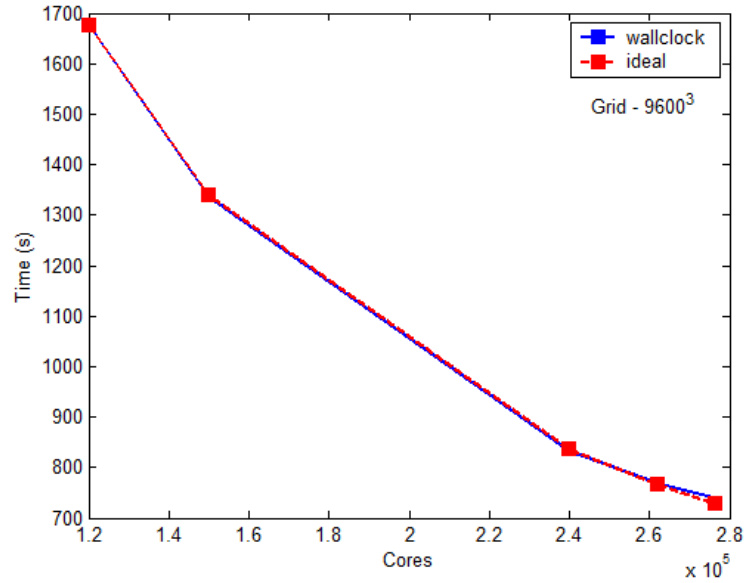| #processors	Wall-clock (s)	Speed-up	Ideal Speed-up
120 000	1674.2	1	1
150 000	1337.4	1.25	1.25
240 000	834.4	2.01	2.00
262 144	769.2	2.18	2.18
276 480	739.4	2.26	2.30

Fig. 7 Strong scaling of the coupled-BEC code on Jaguarpf/Titan CRAY XK-6. The red dots are ideal scaling while the blue dots are our qubit unitary lattice code.

On the IBM/Blue Gene Intrepid, we find similar excellent strong scaling – tested up to 163 840 cores:

Strong Scaling: Grid 4800^3, IBM/Blue Gene (Intrepid)

#processors	Wall-clock (s)	Speed-up	Ideal Speed-up
65 536	1134.5	1	1
98 304	765.0	1.48	1.5
131 072	561.3	2.02	2.0
163 840	455.0	2.49	2.5

Weak scaling is when one changes the grid proportionally to the number of cores so that each processors does the same number of computations. Ideal scaling would result in the wall clock being constant. Again our codes scale excellent under weak scaling on both the CRAY XK-6 and the IBM/Blue Gene

Weak Scaling: CRAY XK-6 (Titan/Jaguarpf)

#processors	Grid	Wall Clock (s)	Ideal (s)
1 728	1200^3	223.5	223.5
13 824	2400^3	224.8	223.5
46 656	3600^3	234.0	223.5
110 592	4800^3	225.7	223.5
216 000	6000^3	231.6	223.5

Weak Scaling : IBM/Blue Gene (Intrepid)

#processors	Grid	Wall Clock (s)	Ideal (s)
64	400^3	425.9	425.9
512	800^3	426.9	425.9
4 096	1600^3	425.5	425.9
32 768	3200^3	421.3	425.9

Work has also been performed on restart i/o using Adios on the CRAY XK-6, and again we are seeing extremely high GB/s being achieved:

Restart i/o (Adios) on the CRAY XK-6 (Titan/Jaguarpf)

Grid	#processors	Write (s)	GB/s (write)	Read (s)	GB/s (read)
1200^3	1 728	3.9	13.2	2.5	20.6
2400^3	13 824	18.0	22.9	22.3	18.5
3600^3	46 656	35.0	39.7	36.0	38.6
4800^3	110 592	75.8	43.5	74.9	44.0

6. 3D Quantum Turbulence

Following Berloff, we can determine the Pade approximant steady state quantum line vortex solution to the GP Eq. (24). In particular for winding number $n = 1$

$$\psi(r,\phi) = e^{i\phi} \sqrt{\frac{11ar^2\left(12 + ar^2\right)}{g\left[384 + ar^2\left(128 + 11ar^2\right)\right]}} \tag{28}$$

where asymptotically: $|\psi| \to g^{-1/2}$ as $r \to \infty$, and $|\psi| \to r a^{1/2} g^{-1/2}$ as $r \to 0$.

Since the GP Eq. (11) is a Hamiltonian system, the total energy of the BEC is a constant:

$$E = E_{kin} + E_{qu} + E_{int} = const. \tag{29}$$

where the total kinetic energy

$$E_{kin} = \frac{1}{2}\int d^3x \rho |\mathbf{u}_s|^2 \quad, \tag{30}$$

the quantum energy (related to the unusual quantum stress tensor)

$$E_{qu} = 2\int d^3x \left|\nabla\sqrt{\rho}\right|^2 \quad, \tag{31}$$

and the interaction energy

$$E_{int} = ag\int d^3x \, \rho^2 \quad. \tag{32}$$

The kinetic energy can be further subdivided into the compressible and incompressible components using the Helmholtz decomposition:

$$E_{kin} = E_{kin}^{COMP} + E_{kin}^{INCOMP} \tag{33}$$

However, since the quantum vortex is a topological singularity we need to regularize the standard definition of velocity and vorticity fields. In particular we work with the density weighted velocity field $\sqrt{\rho}\,\mathbf{u}_s$ to regularize the superfluid velocity at the quantum vortex core.

The development of quantum turbulence can be readily seen in the time evolution of the quantum vortex cores in a run on a 4032^3 grid, Fig. 8

(a) $t = 0$ (b) $t = 400$ (c) $t = 57\,500$
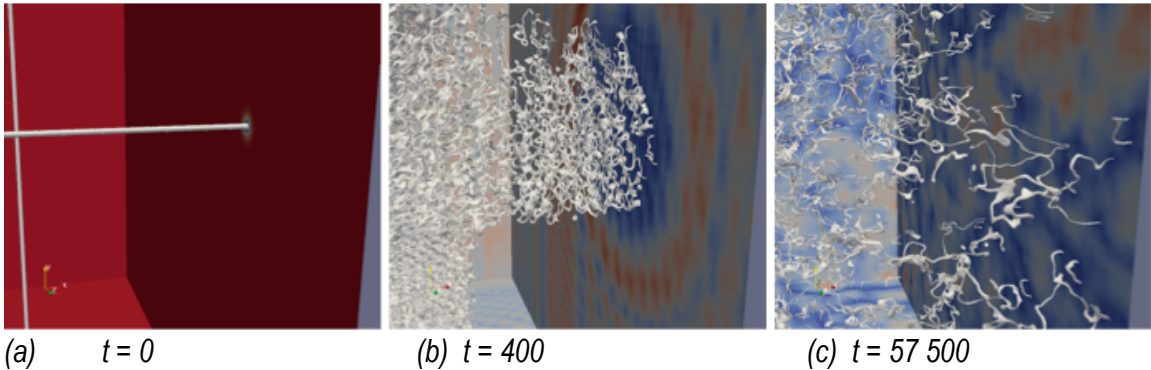
Fig. 8   A zoomed-in section of the GP time evolution of the isosurfaces of 2 quantum line vortex cores (from a total of 12 such vortices) on a spatial grid of 4032^3. (a) At $t = 0$, the vortex core isosurfaces for initial winding number 6 – which is very unstable. By $t = 400$, (b), the cores have expanded and fragmented into $n = 1$ vortices. (c) Vortex tangle is evident at time $t = 57\,500$.

Of much interest is the energy spectra for 3D quantum turbulence. Because of the excellent parallelization of our qubit algorithm, we have received over 6 CAP special user allocations over these past 7 years. This has permitted us to perform production runs on grids not achievable by standard direct CFD solvers. In particular, we have examined the energy spectrum on a 5760^3 grid. Because ofcomputational time constraints, the spectral analysis was performed on MRAP over a 2 week period just after it was acquired and just before it became a classified machine. Hence we could only analyze the total kinetic energy spectrum, Fig. 9.
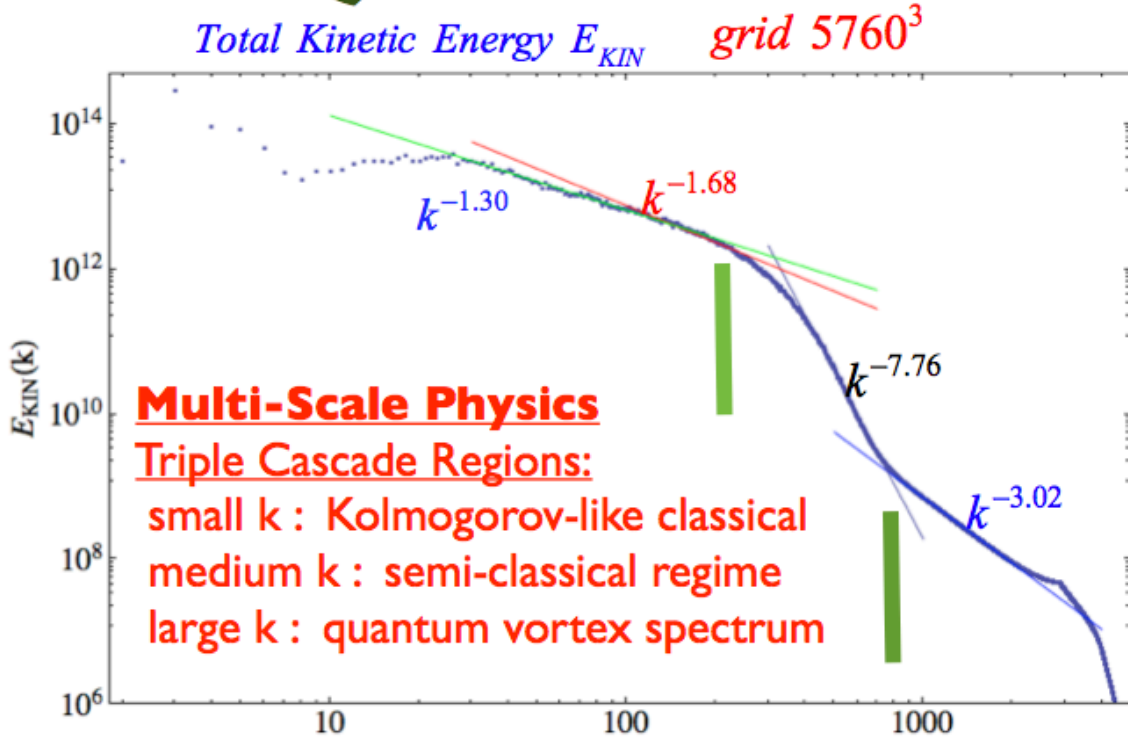
Fig. 9 The total kinetic energy spectrum $E_{kin}(k)$ from a 5760^3 grid simulation. There are 3 clear power law spectral exponents: For large k (800 < k < 2500) $E_{kin}(k) \approx k^{-3}$, for intermediate k (300 < k < 700) a steep $E_{kin}(k) \approx k^{-7.8}$, while for small k (100 < k < 200) $E_{kin}(k) \approx k^{-5/3}$.

While the spectral exponents for the medium and large-k regimes are very robust, there are considerable fluctuations in the small-k spectral exponent (an exponent of -1.30 if one considers the region 30 < k < 175).

A detailed look at the individual energy spectra was performed on grids of 3072^3, and the effect of initial winding number on the line vortices, Figs. 10-11. At t = 0, over 99% of the kinetic energy is in the incompressible mode. However, this rapidly changes, and even by t = 10 K, the triple cascade spectral ranges are readily seen in both $E_{kin}^{COMP}(k)$ and $E_{qu}(k)$. However, the $E_{kin}^{INCOMP}(k)$ spectrum shows only a k^{-3} spectrum over the whole k-range: 30 < k < 1500. As expected, the n = 2 spectra are less noisy for the initial vortices with winding number n = 2 (Fig. 11b compared to Fig. 11a).
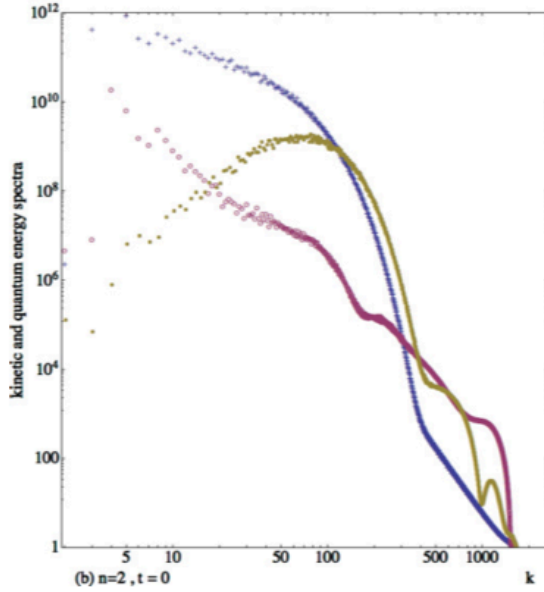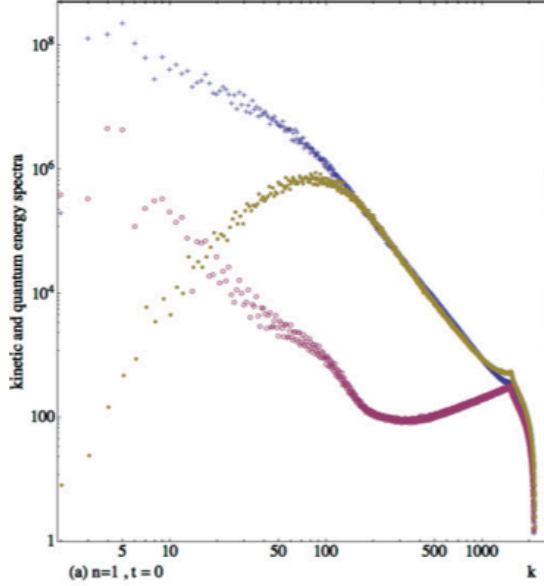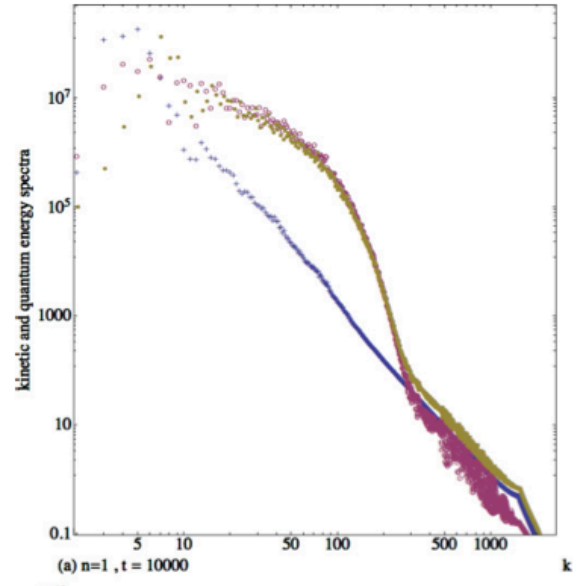
Fig. 10   initial energy spectra   Fig. 11 energy spectra at t = 10 000
    (a) non-degenerate vortices with winding number n=1, (b) degenerate vortices with n = 2.
Color scheme: blue - $E_{kin}^{INCOMP}(k)$, red - $E_{kin}^{COMP}(k)$, gold - $E_{qu}(k)$.

Using linear regression in fixed wave number k windows, we have computed the time averaged energy spectral exponents $\langle\alpha\rangle$, and their average deviation $\pm\langle\sigma\rangle$. The time average is performed on 60 data points from t = 24 000 to t = 48 000 in steps of $\Delta t = 400$

Incompressible Kinetic Energy Spectrum

k-band	$\langle\alpha\rangle$: $E(k)\approx k^{-\langle\alpha\rangle}$	$\pm\langle\sigma\rangle$
15 < k < 90	2.72	0.21
180 < k < 280	3.377	0.021
350 < k < 900	3.006	0.011

Quantum Energy Spectrum

k-band	$\langle\alpha\rangle: \quad E(k)\approx k^{-\langle\alpha\rangle}$	$\pm\langle\sigma\rangle$
15 < k < 90	1.70	0.17
180 < k < 280	7.802	0.058
350 < k < 900	3.033	0.018

Total Kinetic Energy Spectrum

k-band	$\langle\alpha\rangle: \quad E(k)\approx k^{-\langle\alpha\rangle}$	$\pm\langle\sigma\rangle$
15 < k < 90	1.66	0.17
180 < k < 280	8.527	0.064
350 < k < 900	3.042	0.020

We conjecture that for large k > 350 one is basically looking at the intravortex spectrum of a "single" vortex as the incompressible kinetic energy spectrum is a very robust k^{-3}. However, what makes it more complicated is that both the compressible and quantum energy spectra themselves also exhibit a strong k^{-3} - a spectral property clearly not exhibited by a single linear quantum vortex (c.f., Fig. 10). Around $k\approx 350$, both the compressible and quantum energy spectra lift sharply away from the k^{-3} spectrum as we move to smaller k. Around this sharp rise, the incompressible kinetic energy spectrum moves significantly away from k^{-3} to $k^{-3.377}$ for k < 280. Whether this higher exponent is due to Kelvin waves on the vortices needs further investigation. The small k spectral region is also of great interest, since it is tempting to identify this region with the classical Kolmogorov $k^{-5/3}$ kinetic energy spectrum of fluid turbulence. In our quantum turbulence simulations, the incompressible kinetic energy spectrum does not exhibit a $k^{-5/3}$ for small k – but the total kinetic energy does. Interestingly, in subgrid closure models of *compressible classical* fluid turbulence, it is the total subgrid kinetic energy spectrum that is assumed to satisfy the Kolmogorov $k^{-5/3}$ spectrum.

7. 2D Quantum Turbulence

There has been some interest to see whether 2D quantum turbulence would show energy cascade properties like in 3D quantum turbulence or whether it would follow classical physics: in incompressible classical fluid turbulence, there is direct energy transfer from low-k to high-k modes for 3D turbulence while there is an inverse cascade of energy from high-k to low-k modes as in 2D turbulence. Because the quantum vortex is singular at the core, we renormalize the vorticity by weighting it with the density

$$\omega_q = \left[\nabla\times\left(\sqrt{\rho}\,\mathbf{u}_s\right)\right]\cdot\hat{\mathbf{z}} \tag{34}$$

Thus ω_q exhibits the effects of density variations ($\nabla\sqrt{\rho}\times\mathbf{u}_s\cdot\hat{\mathbf{z}}$) as well as the 2D location of the vorticies $\sqrt{\rho}\,\nabla\times\mathbf{u}_s\times\cdot\hat{\mathbf{z}} = \sqrt{\rho}\,\Gamma\,\delta\left(\mathbf{x}-\mathbf{x}_0\right)$. We also consider the density-weighted enstrophy

$$Z = \int d^2x\left|\omega_q\right|^2 \tag{35}$$

It is interesting how vortices are induced in BECs. Experimentally, with sufficient rotation of the BEC, a lattice of vortices is induced within the BEC. Vortices can also be induced by strong Kelvin-Helmholtz instabilities, as we have seen from our simulations, Fig. 12.
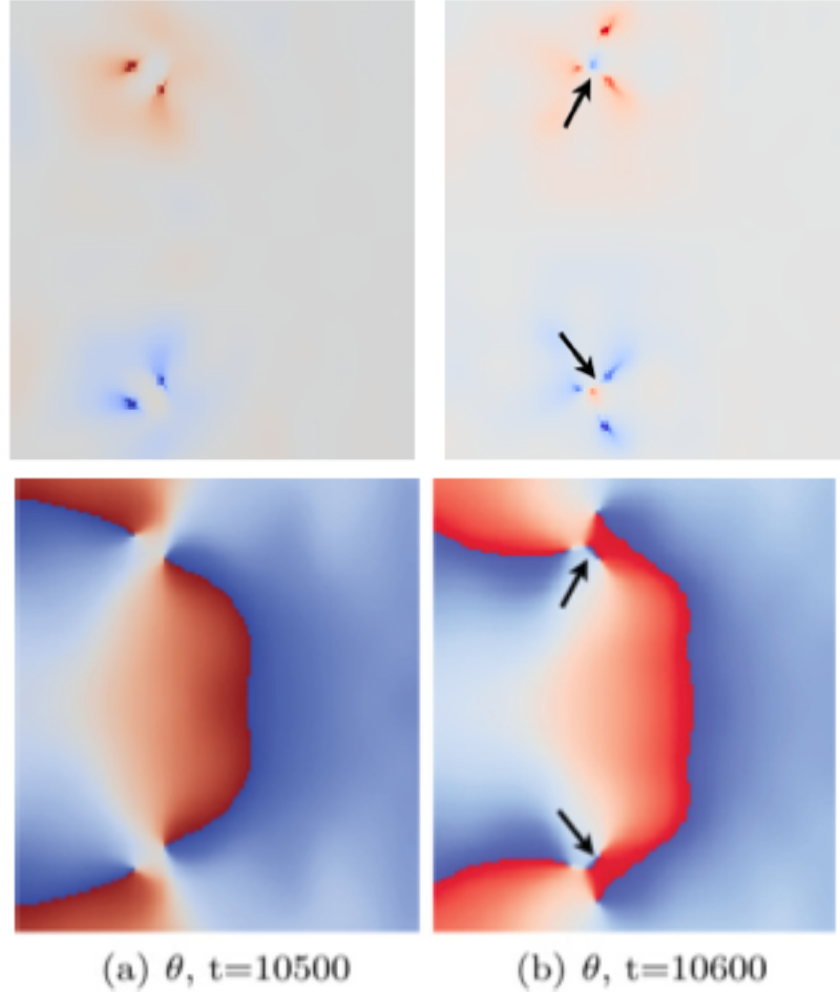

(a) θ, t=10500   (b) θ, t=10600

Fig. 12 The generation of vortex-antivortex pairs in the quantum Helmholtz instability in 2D. The upper plots are for the vorticity $\omega_q(\mathbf{x},t)$ while the lower plots are the corresponding phases of the wave function. (a) at t = 10500, there are 4 vortices present in this 2D spatial region: in the upper plot, the red localized points are for vortices rotating anticlockwise, while the blue localized points are for vortices rotating clockwise. In the lower plots of the wave function phases, blue corresponds to phase 0 while red corresponds to phase 2π. The location of the branch point singularities and the branch cuts are very evident (winding number 1), corresponding to the strong dots seen in the top frame. There is strong shear between the two like-wise rotating vortices, leading to quantum Kelvin-Helmholtz instability and the generation of a pair of clockwise-and-anticlockwise point vortices, as pointed out by the arrows in (b). While the circulation of each vortex is the same, the density weighting around these vortices leads to different strengths of the density-weighted vorticity ω_q.

Another interesting simulation considers the evolution of 2D quantum turbulence from the initial condition of constant density $\rho = const.$, but random phase. Thus initially there are no

quantum vortices (since at a quantum vortex core $\rho=0$).   Since the superfluid velocity is the gradient of this random phase, the initial state is very unstable, and so quantum vortices will rapidly develop.
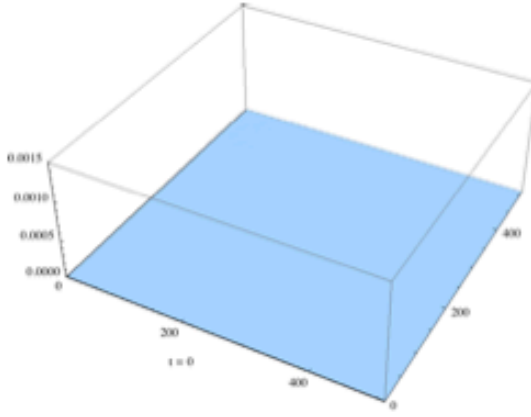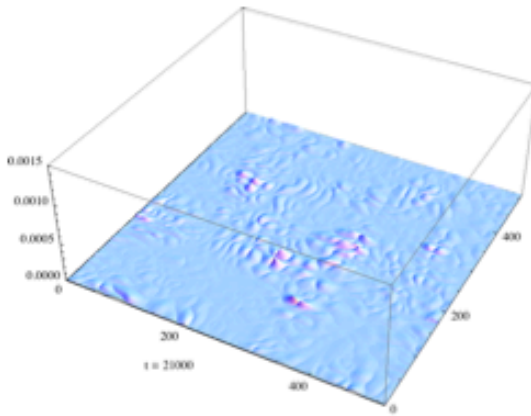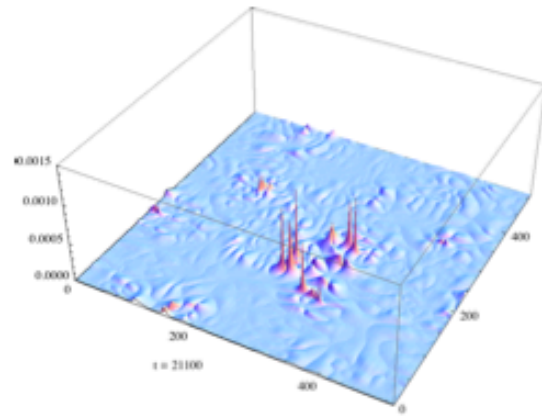

(a) $n = 1, t = 0$
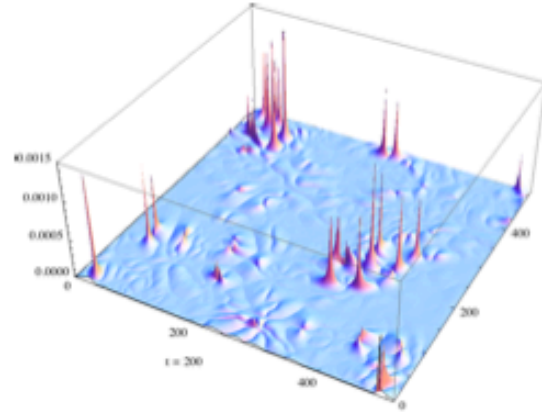
(b) $t = 200$
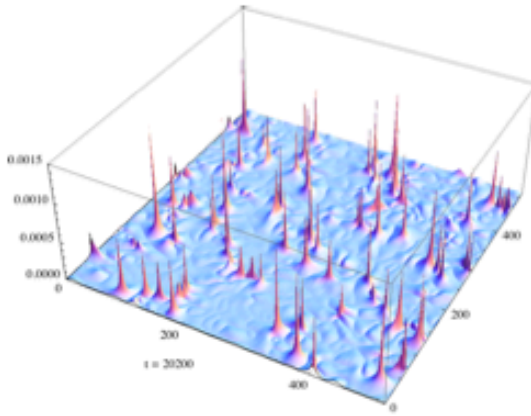
(c) $t = 20200$
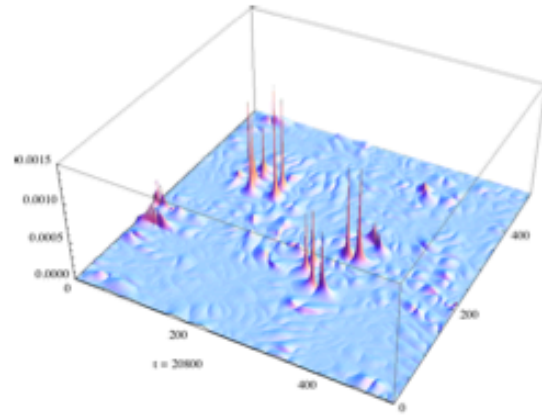
(d) $t = 20800$

(e) $t = 21000 = T_P/2$

(f) $t = 21100$

Fig. 13 The time evolution of the density-weighted vorticity $\left|\omega_q\left(\mathbf{x},t\right)\right|$ *from a constant density, random phase initial condition. At a quantum vortex core* $\omega_q \approx \delta\left(\mathbf{x}-\mathbf{x}_i\right)$. *(a) t = 0, no quantum vorticies since* $\rho\left(\mathbf{x},t=0\right)\neq 0$. *(b)-(d) quantum vortices (* $\delta-function\ spikes$ *) and compressional waves. (e) the onset of a semi-Poincare recurrence in which the vorticity tends to its initial state. There are no quantum vortices, but there are compressional waves. (f) The reappearance of quantum vortices.*

Because the GP system, Eq. (11), is a Hamiltonian system there must be a Poincare recurrence of the initial conditions. However, for almost all continuous systems, this Poincare recurrence time effectively has $T_p \to \infty$. For BECS under certain conditions – particularly when the internal energy << total kinetic energy -- we find remarkably short Poincare recurrence times. Moreover, we find point inversion symmetry of the initial conditions at $T_P / 2$. This is reminiscent of the 2D Arnold Cat Map on the [0,1] square:

$$\begin{pmatrix} x \\ y \end{pmatrix} \to \begin{pmatrix} 2x+y \\ y \end{pmatrix}, \mathrm{mod}\ 1 \tag{36}$$

The Arnold Cat Map is invertible, area preserving, mixing and ergodic with relative short Poincare recurrence time T_P.   Indeed for pixel resolution $\left(300\times300\right)$

(a) t=0   (b) t=150   (c) t=300
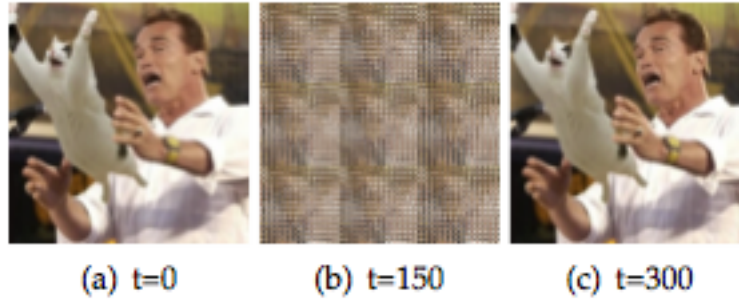
Fig. 14 Poincare recurrence of initial conditions for a particular pixel resolution, 300×300, *for the Arnold Cat Map.*

Yet for other pixel resolutions, one sees a point inversion symmetry at $T_P / 2$:
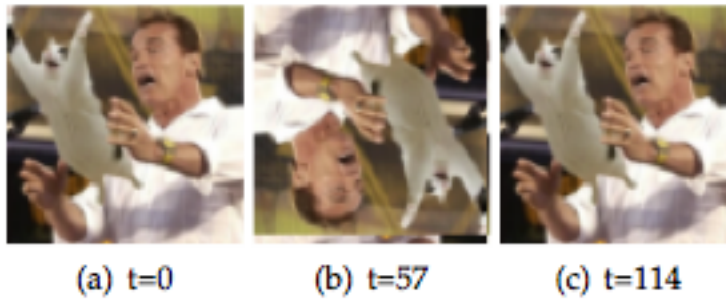

(a) t=0   (b) t=57   (c) t=114

Fig. 15 Poincare recurrence of initial conditions for a pixel resolution, 74×74, *for the Arnold Cat Map. Point symmetry inversion of the initial conditions are now found after* $T_P / 2$ *iterations.*

The precursor to the occurrence of a short Poincare recurrence time for the GP system, Eq. (11), can be seen in the time evolution of the kinetic, quantum and total energies as well as the enstrophy:
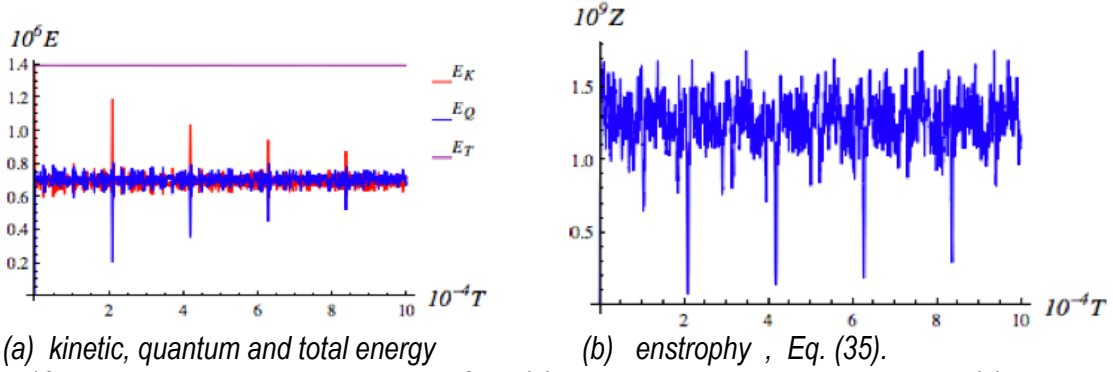
(a) kinetic, quantum and total energy   (b) enstrophy , Eq. (35).

Fig. 16 The spikes in the time evolution of the (a) kinetic and quantum energies, and (b) enstrophy indicate the times of semi-Poincare recurrence for random phase, constant density initial conditions. The strong dips in the enstrophy indicate the depletion of quantum vortices.

However, for stronger internal energies, where

$$\bar{\gamma} = \left\langle \frac{E_{INT}(t)}{E_{KIN}(t)} \right\rangle$$

one finds the destruction of the short Poincare recurrence time, Fig. 17. The average $\langle\ \rangle$ is a time average.

(a) Energy plot for $\bar{\gamma} = 5.67 \times 10^{-2}$ (b) Enstrophy plot for $\bar{\gamma} = 5.67 \times 10^{-2}$

(c) Energy plot for $\bar{\gamma} = 1.33 \times 10^{-1}$ (d) Enstrophy plot for $\bar{\gamma} = 1.33 \times 10^{-1}$
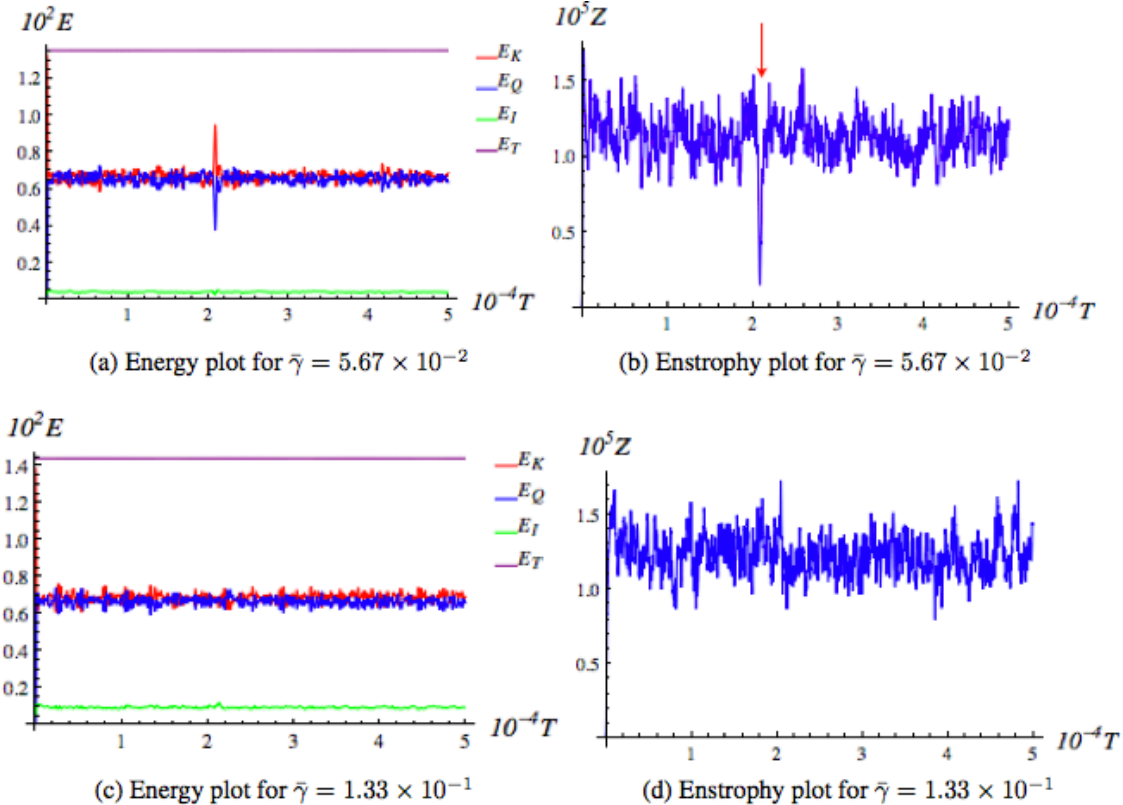
Fig. 17 The loss of the short-Poincare recurrence time as the initial internal energy is increased.

The spectral properties of 2D quantum turbulence is complex. However, all indications are that we do not see inverse cascade of energy to small scales. If we concentrate on the *incompressible* kinetic energy spectrum, then we find the following spectral exponents for 2 runs: one with initial vortices with winding number 1, Fig. 18a, and the other with winding number 2, Fig. 18b.
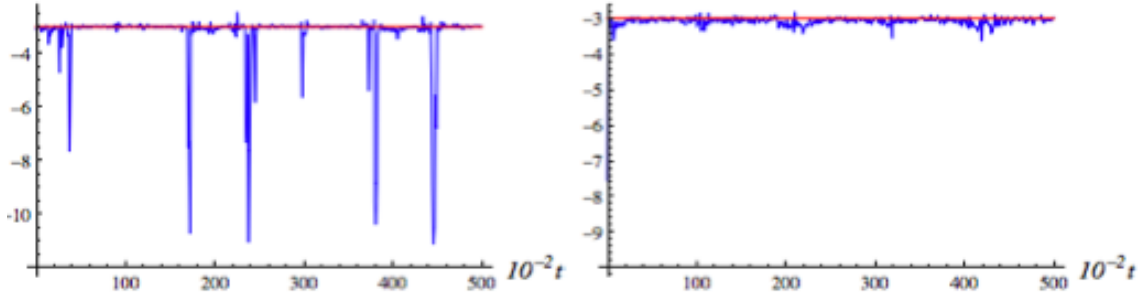

Plot of $s_{IC}(t)$ for   (a) winding number 1   *(b) winding number 2*

Fig. 18 Incompressible kinetic energy spectrum exponent $E_{KIN}^{INCOMP}(k,t) \approx k^{s_{IC}(t)}$. The red line is for the incompressible spectrum with $s_{IC} = -3$: $E_{KIN}^{INCOMP}(k) \approx k^{-3}$. The steep increase in the spectral exponent can be traced to the strong depletion of quantum vortices in the system during that period of evolution of the quantum turbulence. For the more turbulent system with winding number 2, one does not see such a systematic destruction of vortices and hence the incompressible kinetic energy spectrum has only small fluctuations about $s_{IC} = -3$, (b).

(a) t=24400, $s_{ic} = -3.005$ (b) t=24500, $s_{ic} = -5.828$ (c) t=24600, $s_{ic} = -3.357$
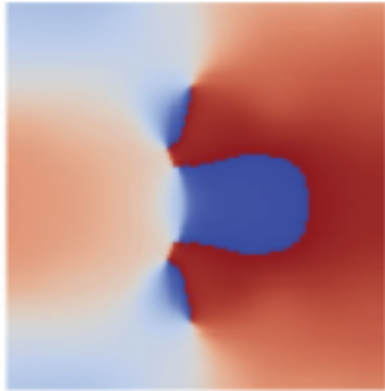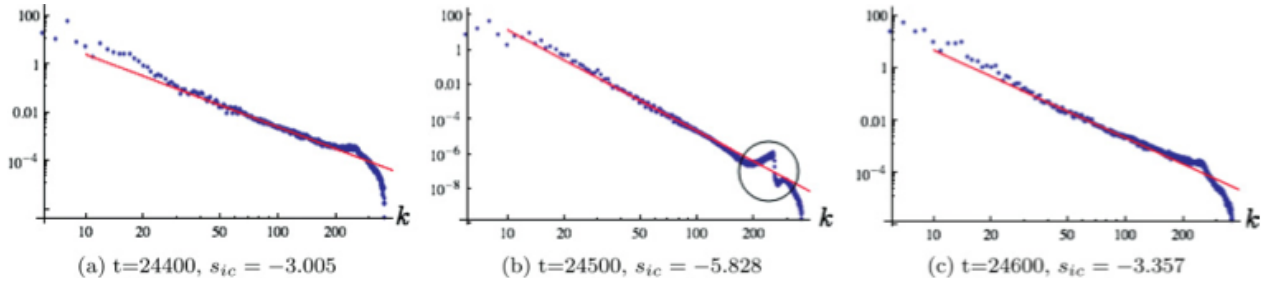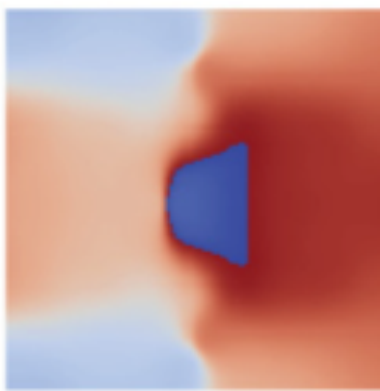
*phases $\varphi(x,y;t)$: (a1) t = 24400*   *(b1)   t = 24500*   *(c1)   t = 24600*
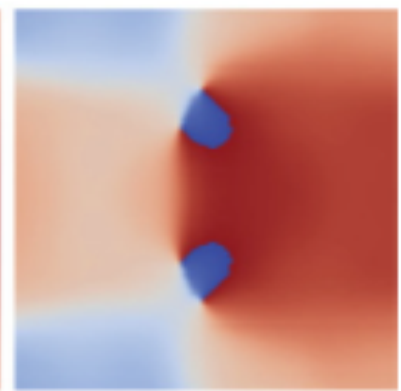
*Fig. 19 The evolution of the **incompressible** kinetic energy spectrum for two neighboring times about the peaking in the exponent $E_{KIN}^{INCOMP}(k) \approx k^{-5.882}$ at t = 24500 , with the strong kink (b) emphasized by the circle in the large-k region. The corresponding blow-up of the phases $\varphi(x,y;t)$ in a very limited spatial subdomain where there are 6 quantum vortices at t = 24400, (a1), **NO** vortices at t = 24500, (b1), and the re-emergence of 4 quantum vortices at t = 24600 .*

A closer look at what is happening about these sharp spectral exponent increases in the incompressible kinetic energy is given in Fig. 19. At t = 24400, (a) and (a1), the incompressible kinetic energy spectrum shows a long range of $E_{KIN}^{INCOMP}(k) \approx k^{-3}$, and we note in the spatial subdomain that there are 6 vortices/branch points with their corresponding branch cuts. By t = 24500, (b) and (b1), the incompressible spectrum has steeped considerably to $E_{KIN}^{INCOMP}(k) \approx k^{-6}$ with a kink for large-k just before the spectrum moves away from a power law. An examination of the same spatial subdomain as in (a1) indicates that the quantum vortices have been destroyed as they are no branch points in (b1). These quantum vortices re-emerge at t – 24600 (actually now 4 quantum vortices) and the incompressible spectrum relaxes again to $E_{KIN}^{INCOMP}(k) \approx k^{-3.4}$.

The 2D quantum spectrum has also been found, for strong winding number degeneracies, to resemble the 3D quantum spectrum – with the **compressible** kinetic energy spectrum exhibiting a triple cascade region, Fig. 20
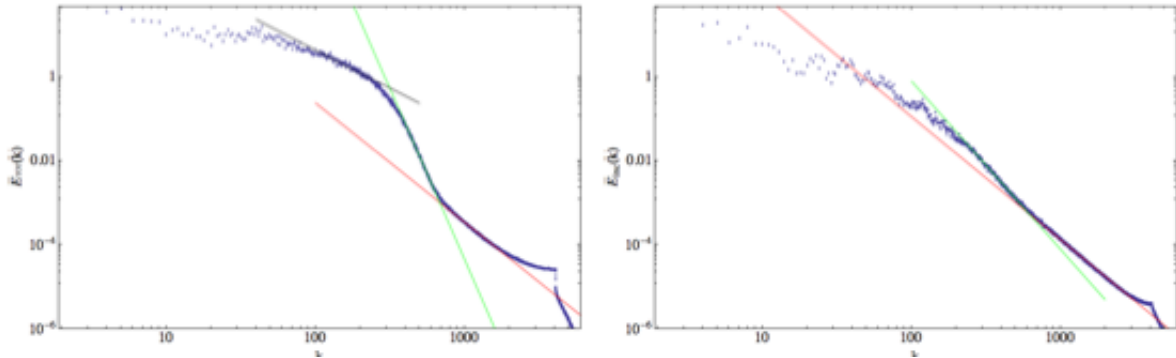
(a) compressible kinetic energy spectrum   (b) incompressible kinetic energy spectrum.

Fig. 20 The kinetic energy spectra for an initial 12 quantum vortex state of degeneracy 6 on a grid of 8192^2 . (a) The compressible spectrum exhibits a triple cascade behavior with exponents $s_C = -1.83$ for small k, $s_C = -8.1$ for intermediate k and $s_C = -2.85$ for large k. (b) The incompressible spectrum has a $s_{IC} = -2.93$ exponent (red), while for an intermediate range we see $s_{IC} = -4.00$ (green).
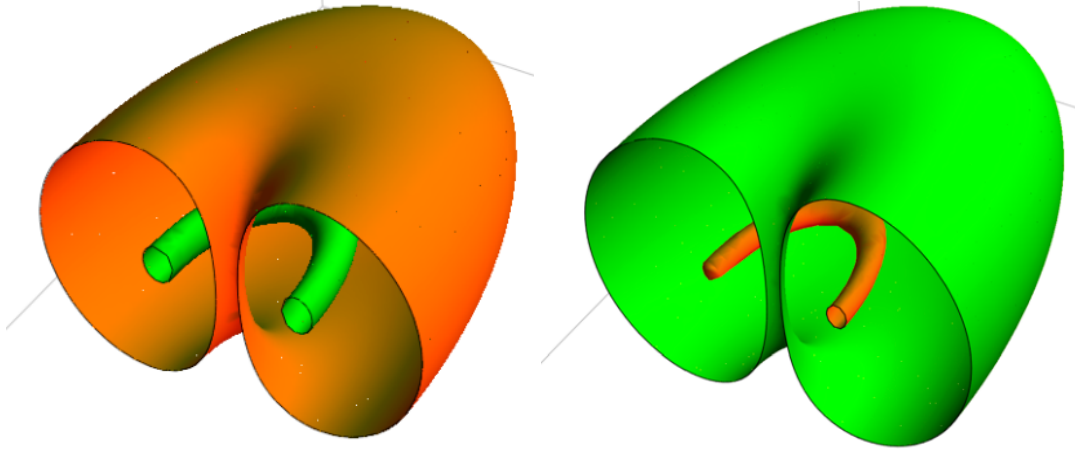
8. Skyrmions

As one moves away from scalar topological defects to higher dimensional ones, we have started to focus on skyrmions. These are localized in space with quantized topological charge – not unlike solitons – and which can undergo interactions and form ordered phases and undergo phase transitions. Such vortices have been produced experimentally using the F = 1 Na condensate. Skyrme (1950's) initially introduced his ideas to explain neutrons and protons as

discrete entities emerging from a continuous field. When quarks entered into the vocabulary in the 1960's, skrymions were neglected and then were again overlooked when string theory became the vogue. However, with the discovery of the quantum Hall effect in the 1990's interest has been rekindled in skyrmions because of the topological properties in the Hall effect and in skyrmions. We consider the skyrmion field as a spinor (in cylindrical coordinates)

$$\Psi = \begin{pmatrix} \psi_+ \\ \psi_- \end{pmatrix} = \begin{pmatrix} \cos\left[\pi\,\tanh(kr) - i\,\frac{z}{r}\,\sin\left[\pi\,\tanh(kr)\right]\right] \\ -i\left[1 - \frac{z^2}{r^2}\right]^{1/2}\,\sin\left[\pi\,\tanh(kr)\right]\,\exp\left[i\theta\right] \end{pmatrix} \tag{37}$$

The vortex cores as well as the asymptotic wave function isosurfaces are shown in Fig. 21

(a) vortex core isosurfaces $\left|\psi_+\right|^2 = 0.04 = \left|\psi_-\right|^2$, (b) asymptotic isosurfaces $\left|\psi_+\right|^2 = 0.9 = \left|\psi_-\right|^2$
Fig. 21 Isosurfaces of the 2-component spinor skyrmion field. (a) The vortex cores are a ring vortex for ψ_+ (green), and for ψ_- (red) a linear vortex along the vertical axis which then closes asymptotically over this apple core at infinity. (b) The asymptotic surfaces interchange roles.

Note that

$$\Psi = \begin{pmatrix} \psi_+ \\ \psi_- \end{pmatrix} = \begin{pmatrix} -1 \\ 0 \end{pmatrix} \quad , \quad as\ \left|\mathbf{x}\right| \to \infty$$

The skyrmion evolution is given by the solution of the spinor GP equation

$$i\frac{\partial \Psi}{\partial t} = -\nabla^2\Psi + a\left(g\left\{\left|\psi_+\right|^2 - \left|\psi_-\right|^2\right\} - 1\right)\Psi \tag{38}$$
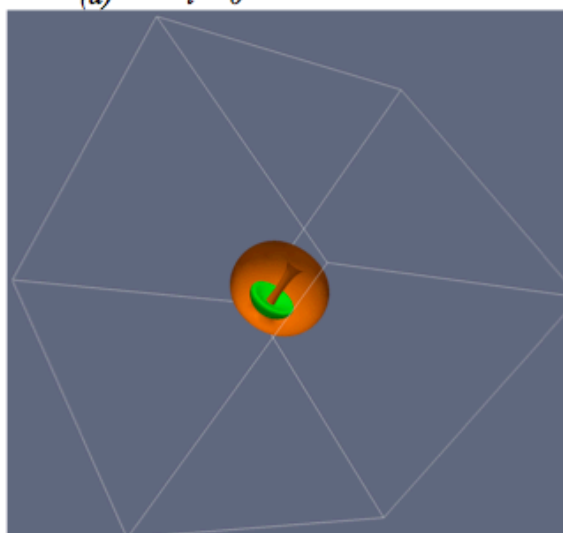
Since we are interested in quantum turbulence, we rescale the skyrmion initial condition , Eq. (37), so that it is not a quasi-eigenfunction for the spinor GP Eq. (38). Hence we see the quantum vortex core of the spinor expand, then interact with the periodic walls to form a percolating lattice of many skyrmions, Fig. 22.
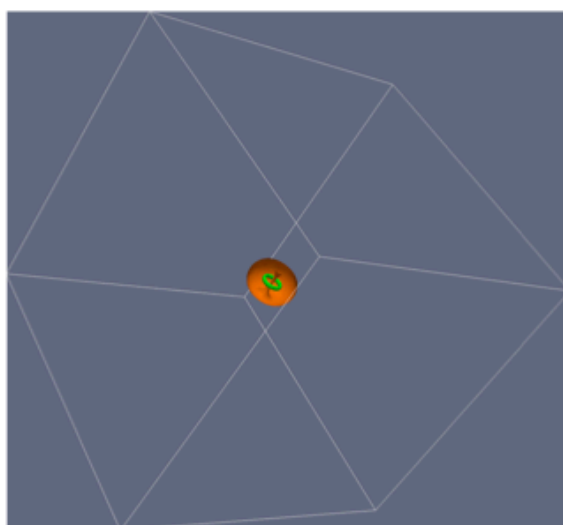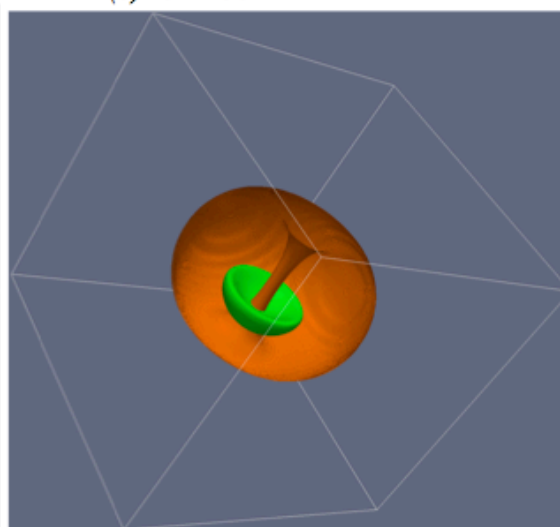
(a)   t = 0
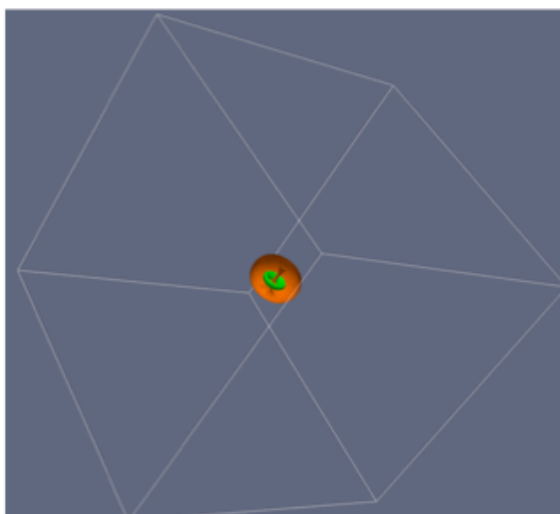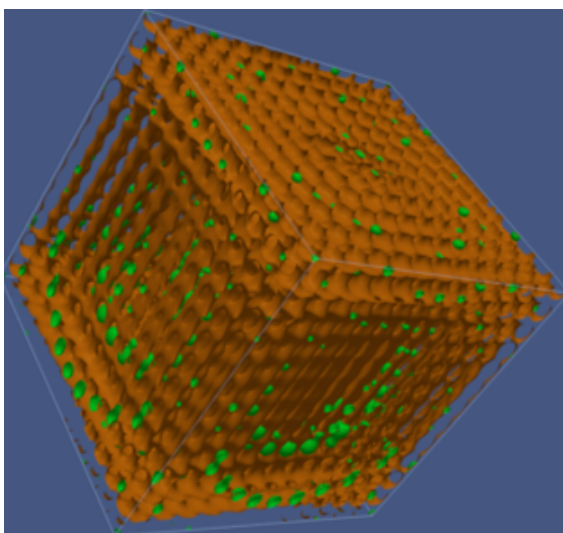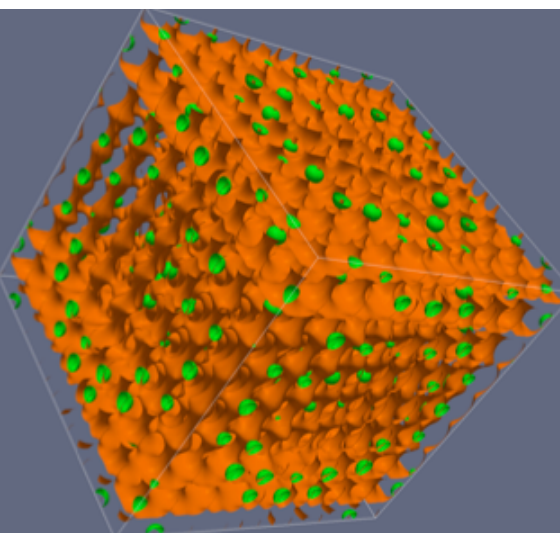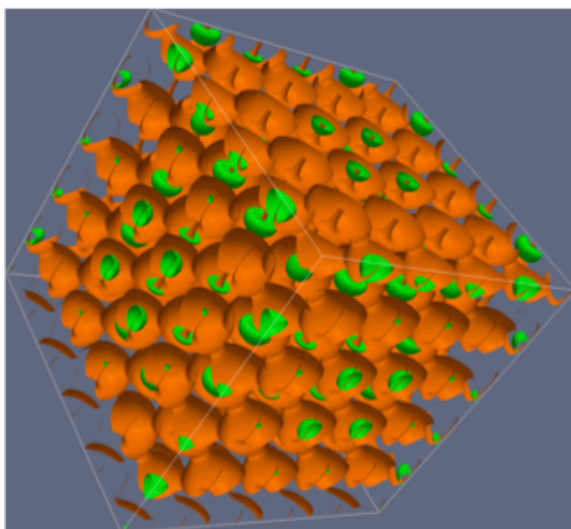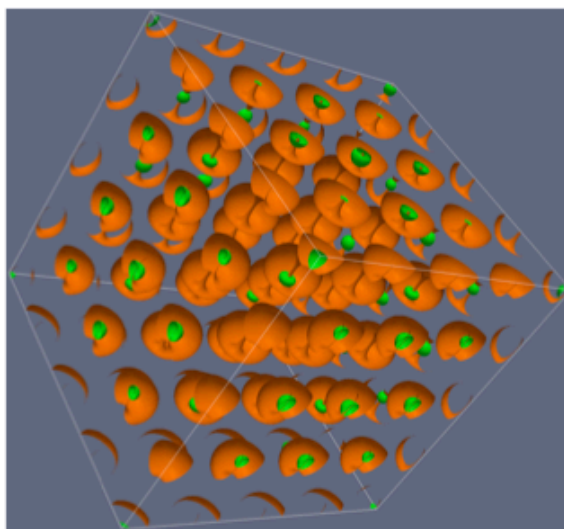
(b)   t = 150

(c)   t = 1000

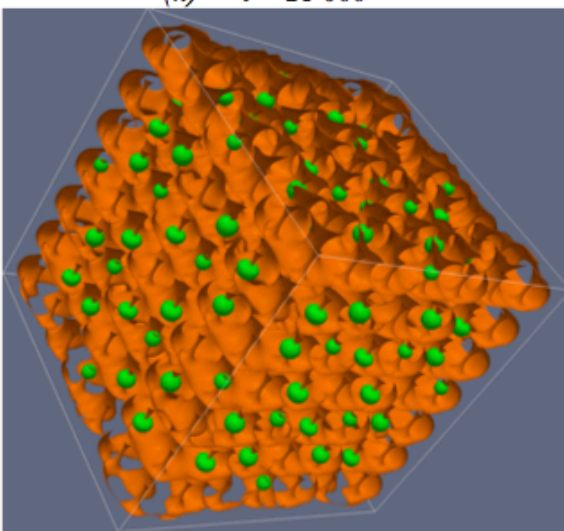(d)   t = 2500

(e)   t = 7000

(f)   t = 10 500

(g)   t = 17 000
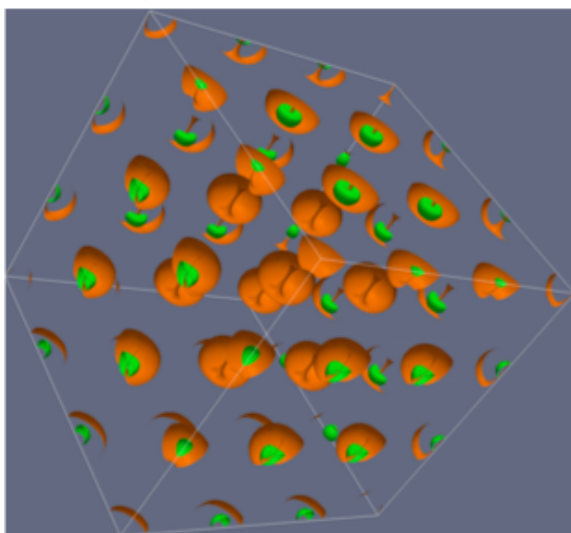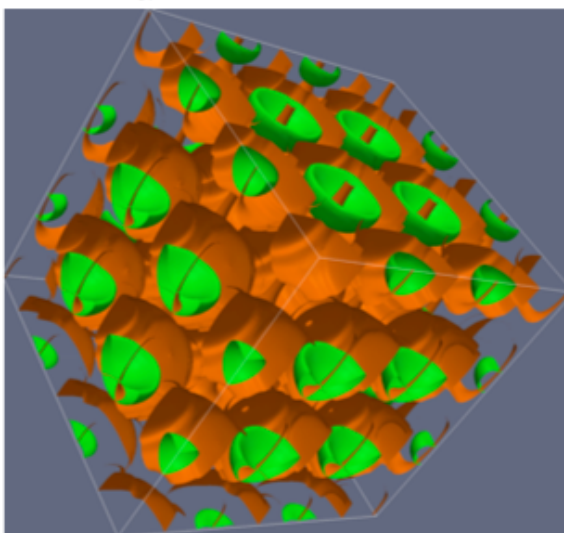
(h)   t = 21 000
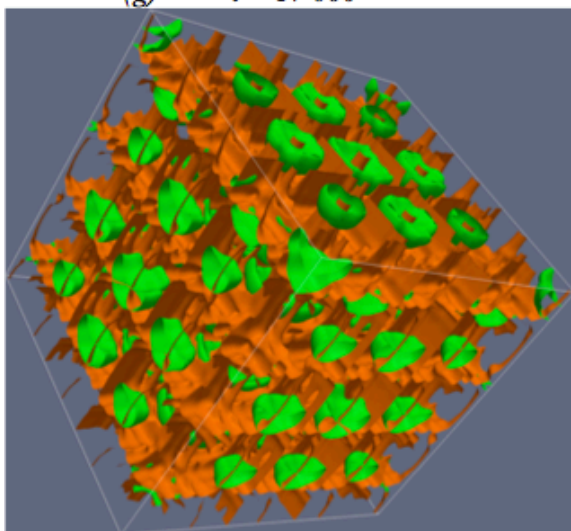
(i)   t = 22 000

(j)   t = 24 000

(k)   t = 28 000

(l)   t = 29 000

Fig. 22   The evolution of the spinor quantum core of a skyrmion under periodic boundary conditions.   The single skyrmion rapidly breaks into a lattice of percolating skyrmions.   These isosurfaces are formed by culling the front interface to expose the innards.   The initial vortex core is a ring vortex for ψ_+ (green) , and for ψ_- (red) a linear vortex along the vertical axis which then closes asymptotically over this apple core.

A snapshot of the spectra for the linear-toroidal vortex core ψ_- (red in Fig. 22) are shown in Fig. 23

(a)   t = 0

(b)   t = 1K
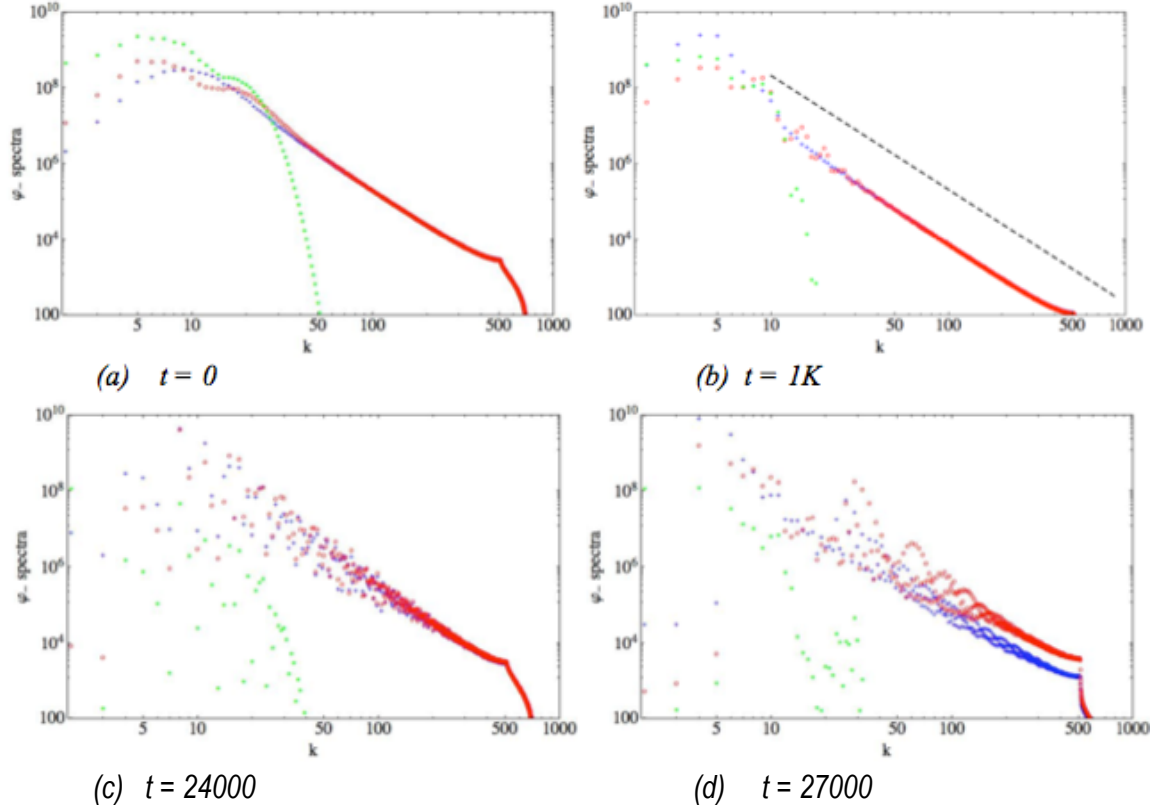
(c)   t = 24000

(d)   t = 27000

Fig. 23   Kinetic energy spectrum (blue), quantum energy spectrum (red) and the internal energy spectrum (green) for the isosurfaces of the spinor component $|\psi_-|$.   The dashed line in (b) is the k^{-3} spectrum.

The spectrum for the vortex ring core ψ_- (green in Fig. 22) is different, and shown in Fig. 24

(a) t = 0

(b) kinetic energy spectrum at 3 times
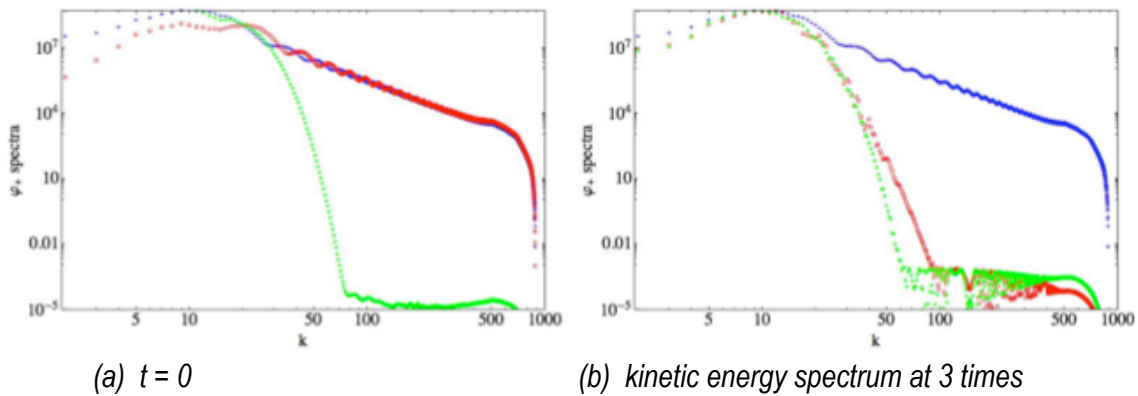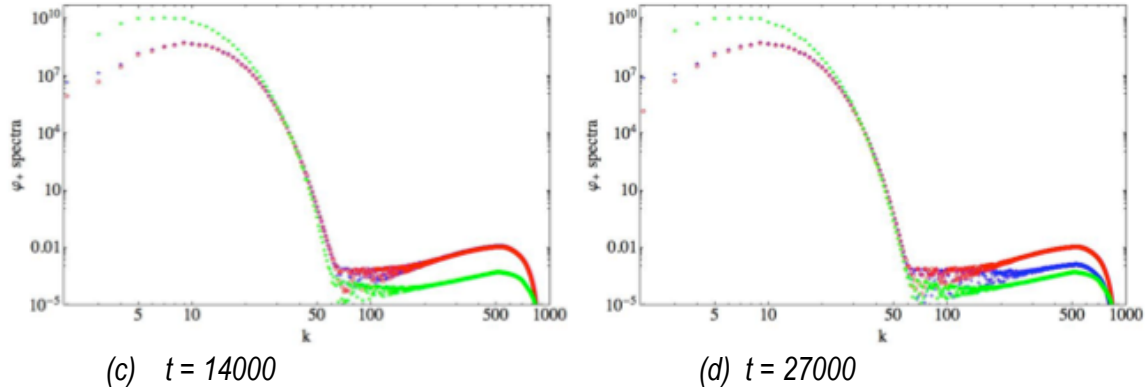
(c)   t = 14000   *(d) t = 27000*

Fig. 24 Kinetic energy spectrum (blue), quantum energy spectrum (red) and the internal energy spectrum (green) for the isosurfaces of the spinor component $|\psi_+|$. While the initial spectra for kinetic and quantum energies exhibit the ubiquitous k^{-3} spectrum, this is rapidly destroyed and followed by steep non-power law dacays. (b) exhibits the rapid destruction of this k^{-3} spectrum for the kinetic energy: t = 0 (blue), t = 1000 (red) , t = 2000 (green).

EDUCATION

Bo Zhang was a graduate student at William & Mary who for his dissertation worked on quantum turbulence in 2D BECs. He graduated with his Ph. D at the end of summer 2011. Currently he is a postdoctoral fellow at the University of Texas at Austin.

PUBLICATIONS 2009 - 2012

G. Vahala, B. Keating, M. Soe, J. Yepez, L. Vahala and S. Ziegeler, "Entropic, LES and boundary conditions in lattice Boltzmann simulations of turbulence", Eur. Phys. J. Special Topics **171**, 167-171 (2009)

J. Yepez, G. Vahala and L. Vahala, "Vortex-antivortex pair in a Bose-Einstein condensate", Eur. Phys. J. Special Topics **171**, 9-14 (2009)

J. Yepez, G. Vahala, L. Vahala and M. Soe, "Superfluid Turbulence from Quantum Kelvin Wave to Classical Kolmogorov Cascades", Phys. Rev. Lett. **103**, 084501 (2009)

G. Vahala, J. Yepez, M. Soe, L. Vahala and S. Ziegeler, "Quantum lattice-gas algorithm for quantum turbulence: CAP simulations using 12,288 cores on the CRAY XT-5 (*Einstein*) at NAVO, IEEE Computer Society (2009).

J. Yepez, G. Vahala and L. Vahala, "Quantum algorithm for Bose-Einstein condensate quantum fluid dynamics: Twisting of filamentary vortex solitons demarcated by fast Poincare recursion", SPIE Quantum Information and Computation, Vol. 7342-21, 73420M (2009), 10 pages.

G. Vahala, J. Yepez, L. Vahala, M. Soe and S. Ziegeler, "Poincare Recurrence and Intermittent Destruction of the Quantum Kelvin Wave Cascade in Quantum Turbulence", Proc. SPIE Quantum Information and Computation, Vol. **7702**, 770207 (2010)

J. Yepez, G. Vahala, L. Vahala and M. Soe, Phys. Rev. Lett. **105,** 129402 (2010)

B. Zhang, G. Vahala, L. Vahala, M. Soe, "Unitary quantum lattice gas representation for 2D quantum turbulence", Proc. SPIE **8057**, 80570E1-12 (2011) - 4 pages

B.Zhang, G. Vahala, L. Vahala, M. Soe, "Unitary quantum lattice algorithm for two-dimensional quantum turbulence", Phys. Rev. **E84**, 046701 (2011) - 13 pages

G.Vahala, J. Yepez, L. Vahala, M. Soe, B. Zhang and S. Ziegeler, "Poincare recurrence and spectral cascades in three-dimensional quantum turbulence", Phys. Rev. **E84**, 046713 (2011) - 17 pages

G. Vahala, M. Soe, B. Zhang, J. Yepez, J. Carter and S. Ziegeler, "Unitary qubit lattice simulations of multiscale phenomena in quantum turbulence", Supercomputing 2011, paper TCC304, Nov. 2011 (Seattle) -10 pages

G. Vahala, B. Zhang, J. Yepez, L. Vahala and M. Soe, "Unitary qubit lattice gas representation of 2D and 3D quantum turbulence", Chpt 11 in *"Advanced Fluid Dynamics"* , ed. H. W. Oh (InTech Publishers, 2012), pp. 239-272

G. Vahala, J. Yepez, L. Vahala and M. Soe, "Unitary qubit lattice simulations of complex vortex structures:, Computat. Science and Discovery **5**, 014013 (2012) - 19 pages.